Unconventional free charge in the correlated semimetal $Nd_2Ir_2O_7$

K. Wang[1], B. Xu[2], C. W. Rischau[1], N. Bachar[1], B. Michon[1], J. Teyssier[1], Y. Qiu[3], T. Ohtsuki[3], Bing Cheng[4], N. P. Armitage[4], S. Nakatsuji[3,4,5,6] and D. van der Marel[1]✉

$Nd_2Ir_2O_7$ is a correlated semimetal with the pyrochlore structure, in which competing spin–orbit coupling and electron–electron interactions are believed to induce a time-reversal symmetry-broken Weyl semimetal phase characterized by pairs of topologically protected Dirac points at the Fermi energy[1-4]. However, the emergent properties in these materials are far from clear, and exotic new states of matter have been conjectured[5-7]. Here, we demonstrate optically that, at low temperatures, the free carrier spectral weight is proportional to T^2, where T is the temperature, as expected for massless Dirac electrons. However, we do not observe the corresponding T^3 term in the specific heat. That the system is not in a Fermi liquid state is further corroborated by the charge carrier scattering rate approaching critical damping and the progressive opening of a correlation-induced gap at low temperatures. These observations cannot be reconciled within the framework of band theory of electron-like quasiparticles and point towards the effective decoupling of the charge transport from the single particle sector.

Topological metallic states in correlated systems with strong spin–orbit coupling are an active field of research that, in recent years, has led to the observation of a topological Kondo insulator in SmB_6 (refs. [8,9]), a magnetic Weyl semimetal in Mn_3Sn (refs. [10,11]) and a Weyl Kondo phase in $Ce_3Bi_4Pd_3$ (ref. [12]) and $CeRu_4Sn_6$ (ref. [13]). Of particular interest in this context are the transition metal oxides with the pyrochlore structure, which have the composition $Ln_2Ir_2O_7$, where Ln is usually a trivalent rare-earth ion. The primitive cell contains two formula units, that is four Ir ions, with the Ir–O–Ir bonds forming a frustrated network of corner-sharing tetrahedra. At high temperatures, these materials are paramagnetic semimetals where a pair of doubly degenerate bands of opposite curvature have a quadratic band touching (QBT) point at the centre of the Brillouin zone[6,14,15] that at zero doping is coincident with the Fermi level and the Fermi surface is a single point. At low temperatures, these materials were predicted[1] and have been observed[16–21] to order magnetically with all the Ir 5*d* moments pointing inward or outward from the centre of the tetrahedron. This order does not affect the translational symmetry of the system, but because it breaks the time-reversal symmetry, the double degeneracy of the bands is lifted, giving rise to four non-degenerate bands[1]. Simultaneously, the zone-centre QBT transforms into 12 pairs of Weyl nodes, making for a grand total of 24 Weyl nodes[1]. These nodes act as a source or sink of Berry curvature, and are topologically protected. Increasing the on-site Coulomb interaction shifts the Weyl nodes away from the zone centre towards the Brillouin zone boundary, until the two members of each pair meet at the zone boundary, where they mutually annihilate and a correlation-induced gap opens[1,2,7,22–26]. Ueda and others have confirmed the presence of a gap at low temperatures in the optical spectrum of polycrystalline $Nd_2Ir_2O_7$ (refs. [27,28]). Indications of Weyl semimetal behaviour have been reported in the optical spectra of the related compound $Eu_2Ir_2O_7$ (refs. [4,29,30]) at low temperatures.

We have measured and analysed the transport, specific heat, magnetic susceptibility and optical spectroscopic data of single-crystalline $Nd_2Ir_2O_7$. Experimental details are described in the Methods. Figure 1 presents the d.c. conductivity, susceptibility, specific heat and low-energy optical conductivity data, while Fig. 2 shows the optical conductivity on an expanded scale. Fitting the reflectivity and ellipsometry data to a Drude–Lorentz model provided the plasma frequency, $\omega_p(T)^2$, of the zero-energy mode displayed in Fig. 2a. The free carrier weight shows a T^2 temperature dependence with a small zero-temperature offset, $\omega_p(0)^2$. For a system with g Dirac cones at the Fermi level, it is expected that[31,32]

$$\omega_p(T)^2 = \omega_p(0)^2 + \frac{2\pi\alpha}{9}\frac{gc}{v}(k_B T)^2$$

where α is the fine-structure constant, c is the velocity of light in vacuum, v the Dirac velocity, and k_B is the Boltzmann constant. Following ref. [1], we will assume that there are 12 Weyl pairs, that is $g=24$. The experimental data in Fig. 2a then imply that $v=3.1\,\mathrm{km\,s^{-1}}$. The $\omega_p(0)^2$ term indicates the presence of doped charge carriers and, for the aforementioned values of g and v, corresponds to 0.003 carriers per Ir ion and $|\mu|=1.0\,\mathrm{meV}$ (Methods and equations (16) and (17)), where μ is the chemical potential. This small value of $|\mu|$ may imply that, following the argument of Moon et al., the Coulomb interaction can convert the paramagnetic QBT into a quantum critical non-Fermi liquid[6]. The optical conductivity of polycrystalline $Nd_2Ir_2O_7$ shows a somewhat more pronounced gap at low temperatures and a smaller weight of the zero-energy mode, but the temperature dependence of the spectral weight of the zero-energy mode was not addressed[27].

The value of the Dirac velocity v is extremely small, even below typical values of the sound velocity in solids and only six times higher than the sound velocity in cork[33]. For a band dispersing from the zone centre to the L point with the same velocity, this corresponds to a bandwidth of only 12 meV. Because the entropy and specific heat of 3D Dirac fermions are proportional to T^3/v^3

[1]Department of Quantum Matter Physics, University of Geneva, Geneva, Switzerland. [2]Department of Physics and Fribourg Center for Nanomaterials, University of Fribourg, Fribourg, Switzerland. [3]Institute for Solid State Physics, The University of Tokyo, Kashiwa, Japan. [4]The Institute for Quantum Matter and the Department of Physics and Astronomy, The Johns Hopkins University, Baltimore, MD, USA. [5]CREST, Japan Science and Technology Agency, Kawaguchi, Saitama, Japan. [6]Department of Physics, University of Tokyo, Hongo, Bunkyo-ku, Tokyo, Japan. ✉e-mail: dirk.vandermarel@unige.ch

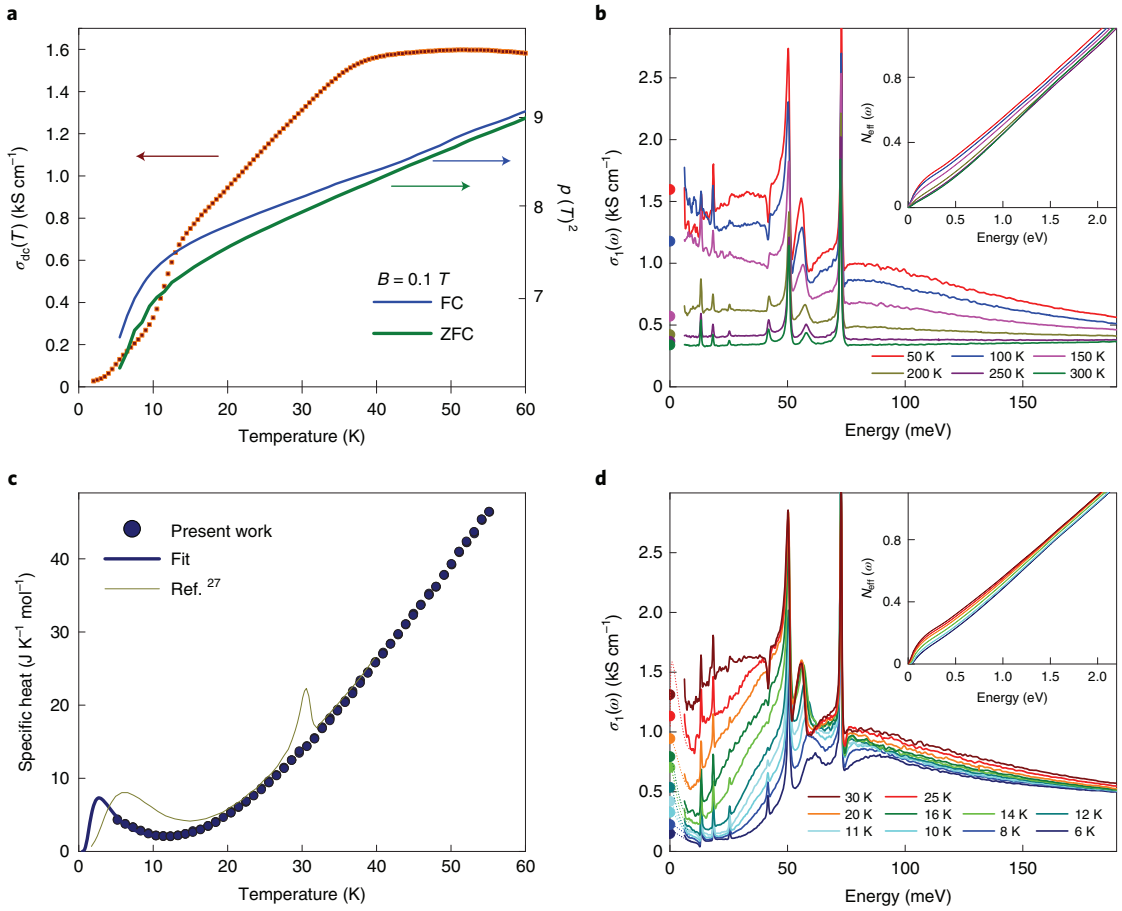

Fig. 1 | Experimental transport and optical conductivity data of $Nd_2Ir_2O_7$. a, D.c. conductivity (brown symbols). Blue and green curves are, respectively, the zero-field-cooled (ZFC) and field-cooled (FC) temperature dependence of the squared effective moment per Nd ion, $p(T)^2 \equiv (V_{pc}/4)\chi(T)3k_BT/\mu_B^2$, where k_B is the Boltzmann constant, μ_B is the Bohr magneton, V_{pc} is the volume of the primitive cell and $\chi(T)$ is the magnetic susceptibility (see Methods and equation (1)). If the Curie law applies, one should expect $p(T)^2 = 13.1$ at all temperatures, corresponding to the local moment of a Nd^{3+} ion. The decrease of $p(T)^2$ with decreasing temperature reveals the departure from the Curie law as a result of exchange coupling of the magnetic ions. **b**, Optical conductivity of $Nd_2Ir_2O_7$ at selected temperatures above 37 K. **c**, Dark blue circles are the present specific heat data. The dark blue solid curve is a fit to equation (5) (see Methods) with a separation between ground state and first excited state $\Delta_0 = 6.5$ K. The dark yellow curve is the specific heat of polycrystalline $Nd_2Ir_2O_7$ digitized from data in fig. 1 of ref. [27]. **d**, Optical conductivity of $Nd_2Ir_2O_7$ at selected temperatures below 37 K. Filled circles along the ordinates of **b** and **d** represent the d.c. conductivity using the four-terminal method. Insets in **b** and **d**: effective number of electrons per primitive cell (Methods and equation (3)).

(see Methods and equations (10) and (11)), one would expect that such a low velocity causes the release of an enormous amount of entropy when the temperature is raised, even exceeding the acoustic phonon contribution. Because the optical conductivity of Dirac electrons is proportional to ω/v (see Methods and equation (14)), we should also observe a high, linear-in-frequency, infrared conductivity. In Fig. 2 we compare these estimates with the experimentally measured $s(T)$and $\sigma_1(\omega)$, and we see that the experimental values fall an order of magnitude below the calculation for $v = 3.1\,\mathrm{km\,s^{-1}}$ (brown dashed line). The interband optical conductivity data at 16 K come closest to a linear frequency dependence and can be fitted with $v = 41\,\mathrm{km\,s^{-1}}$ (green dash-dotted line). This extrapolates to 150 meV at the zone boundary and falls in the range of the 100–200 meV band dispersion calculated with the LDA+U method[1,23]. Regarding the specific heat data, a quantitative comparison of the contributions from phonons, localized Nd 4*f* electrons and itinerant Ir 5*d* electrons shows that (1) below 15 K, the specific heat is dominated by the localized Nd 4*f* electrons, (2) above 15 K, the specific heat is dominated by the phonons and (3) at all temperatures, the contribution from the itinerant Ir 5*d* electrons is negligible. Consequently, an entropy of Weyl fermions with $v = 3.1\,\mathrm{km\,s^{-1}}$, as suggested by the result for $\omega_p(T)^2$ shown in Fig. 2a, would far exceed the experimentally obtained entropy. The present data and those of ref. [27] show a perfect match above the Néel temperature T_N, but, possibly due to the different types of sample (for example, single crystal versus polycrystal), the Schottky anomaly, Néel temperature and specific heat jump at T_N are significantly different. These differences are inter-related: T_N being higher and the Schottky anomaly occurring at a lower temperature together cause the jump at T_N to vanish against the phonon background (see Methods).

This leaves us with a strange conundrum. In a single-electron model, the T^2 temperature dependence of the free carrier spectral weight is due to thermal activation of free carriers. However, the specific heat data do not show the corresponding $S = -k_B\sum_k \left[f_k \ln f_k + (1-f_k)\ln(1-f_k)\right]$ entropy release. We therefore infer that the observed $\omega_p^2 = aT^2$ temperature dependence does not reflect the statistical properties of non-interacting electrons. This state of affairs calls for a radically different interpretation of the experimental data, to which we return in the following.

We now turn to the $\sigma_{dc}(T)$ data. Hosur et al.[34] predicted a linear temperature dependence of $\sigma_{dc}(T)$ for Weyl nodes in the presence of the Coulomb interaction. The experimental data in Fig. 1a

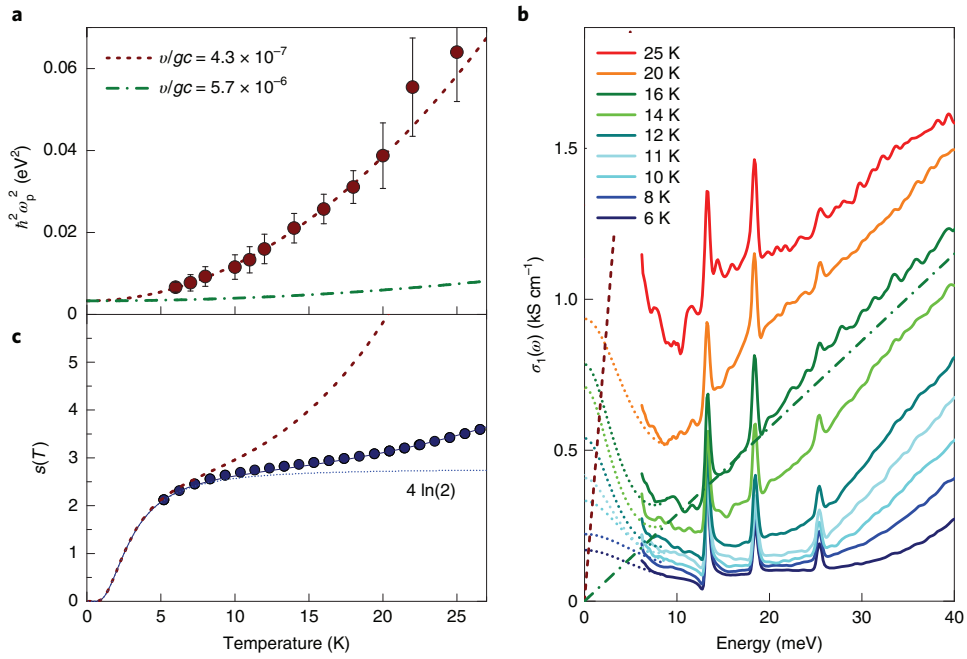

Fig. 2 | Comparison and analysis of the free charge spectral weight, entropy and low-energy optical conductivity of $Nd_2Ir_2O_7$. a, Brown circles: temperature dependence of the experimentally obtained free carrier spectral weight. Error bars were obtained by shifting the reflectivity data 4% up and down relative to the measured values. Brown and green dashed curves show theoretical values (see Methods and equation (15)) for g Weyl nodes in the first Brillouin zone with velocity $v/gc = 4.3\times10^{-7}$ and 5.7×10^{-6}, respectively, where c is the velocity of light in vacuum. **b**, Optical conductivity for selected temperatures. The dark green dash-dotted and brown lines show the theoretical $\sigma_1(\omega)$ (see Methods and equation (14)) for $v/gc = 5.7\times10^{-6}$ and 4.3×10^{-7} respectively. **c**, Entropy per primitive cell (two formula units of $Nd_2Ir_2O_7$) in units of k_B. The dark blue curve shows integration of the fit to the experimental specific heat data of Fig. 1, using equation (4) from the Methods. The blue circles show integration of the experimental data of Fig. 2. The dotted blue line shows the Schottky contribution. The brown dashed curve shows the sum of the Schottky contribution and the theoretical prediction for Weyl fermions (see Methods and equation (11)) with velocity $v/gc = 4.3\times10^{-7}$.

indeed show a striking linear temperature dependence between 15 and 37 K, but there is a finite zero-temperature intercept. The Drude relation $4\pi\sigma_{dc}(T) = \omega_p^2\tau$, where τ is the relaxation time, together with the temperature dependence of ω_p^2 in Fig. 2a, then implies

$$\hbar/\tau \leq Ak_BT$$

with the dimensionless coefficient $A = 0.23$. The inequality becomes an equality if we assume that the zero-temperature intercept of $\sigma_{dc}(T)$ comes from parallel shunting by doped carriers and that their conductivity is independent of temperature. Either way, the scattering rate approaching the 'Planckian'[35] value k_BT signals that the thermal charge excitations approach the limit of being critically damped. For $T < 13$ K, the d.c. conductivity drops below the linear temperature dependence, while leaving unaffected the T^2 dependence of ω_p^2. It is peculiar that, despite a manifest change of behaviour of $\sigma_{dc}(T)$ at 13 K, the free charge spectral weight follows a smooth T^2 dependence in the entire temperature range from 6 to 25 K, beyond which it becomes too strongly mixed with the interband transitions. This implies that the sudden drop of $\sigma_{dc}(T)$ below 13 K is caused by some form of localization of the charge carriers, with no discernable influence on the spectral weight ω_p^2. This behaviour signals a crossover toward a state of matter characterized by an increased momentum transfer scattering. Because this overlaps with the temperature range of the Schottky anomaly of the Nd ions in the specific heat (Fig. 1), it is possible that the observed scattering has—at least in part—to do with scattering by the Nd magnetic moments, as was suggested by Ueda and colleagues[27]. Scattering of the itinerant Ir 5*d* electrons from the rare-earth moments was also not observed in $Pr_2Ir_2O_7$, a related pyrochlore $Ln_2Ir_2O_7$ system that does not order

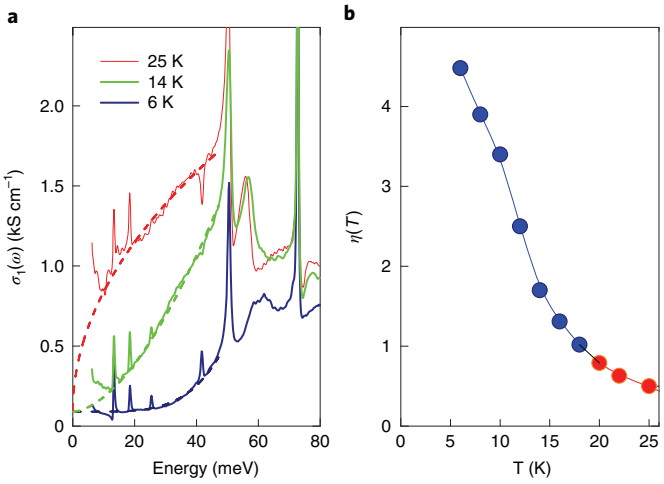

Fig. 3 | Power-law analysis of the interband transitions of $Nd_2Ir_2O_7$. **a**, Optical conductivity of $Nd_2Ir_2O_7$ with fits to the power law form $\sigma_1(\omega) = \sigma_0 + a\omega^\eta$ with $\sigma_0 = 90$ S cm^{-1}. **b**, Temperature dependence of the exponent η. Blue and red coloured circles indicate temperature regions where $\sigma_1(\omega)$ is superlinear and sublinear, respectively.

at low T (ref. [15]). The observed Schottky anomaly can be fitted to a two-level system at each Nd site having a high temperature limiting $k_B\ln(2)$ entropy with the ground-state and first excited state separated by $\Delta_0 = 6.5$ K (Fig. 1). Because this is much smaller than the 26-meV (ref. [36]) crystal field splitting between the two lowest

doublets of the the $J=9/2$ manifold, the splitting $\Delta_0=6.5$ K signals the lifting of the degeneracy within the ground-state doublet. This requires a static exchange field at the Nd sites and is a clear indication that the time-reversal symmetry is broken. The freezing of Nd moments may foster opening the Mott gap of the 5*d* bands[2], and the exchange fields then open the charge gap in $Nd_2Ir_2O_7$.

We observe in Figs. 1 and 2 that the interband optical conductivity below 80 meV is strongly temperature-dependent for the entire temperature range below 37 K down to the lowest measured temperature of 6 K. For most temperatures, the spectral shape corresponds neither to $\sigma_1(\omega)\propto\omega^{0.5}$ (3D quadratic band touching) nor $\sigma_1(\omega)\propto\omega$ (3D Dirac cone). Instead, the evolution as a function of temperature is phenomenologically described by the gradual evolution with temperature of a general power law, $\sigma_1(\omega)\propto\omega^{\eta}$, as shown in Fig. 3. The temperature dependence of $\eta(T)$ reveals a gradual and strong increase from 0.5 at 25 K to 4.5 at 6 K, with an inflection point around 13 K. This evolution of $\eta(T)$ with temperature corroborates what is already obvious from direct inspection of the $\sigma_1(\omega)$ spectra, namely that, on cooling below 37 K, a depletion takes place of the low-energy interband transitions, consistent with the gradual (second-order) transition into the Weyl semimetal phase. The spectral weight removed from low frequencies, rather than being recovered at energies directly above the gap, is transferred to a broad energy range above 1 eV. We attribute this anomalous transfer to the 'Mottness' of this system, that is, a sensitivity to local interactions and proximity to a Mott insulating phase[5,37]. Interestingly, the η in Fig. 3 remains in the region between 0.5 and 1 when cooling from $T_N=37$ K to 18 K. The inflection point around 13 K signals the appearance of the correlation-gapped Weyl semimetal phase (or 'Weyl Mott insulator'[7]).

The observation of a T^2 zero-energy spectral weight in the optical conductivity, without an appreciable entropy contribution, is difficult to understand. To illustrate that no general one-to-one relation exists between the entropy of the free carriers and their spectral weight, we consider a non-interacting model of a semimetal for which at $T=0$ the bands touch at the Fermi energy E_F so that free carrier spectral and entropy are both zero. If, by tuning the crystal structure at $T=0$, the bands start to overlap, the free carrier spectral weight becomes finite, while the entropy remains zero. A priori, we cannot rule out such a change of electronic structure as a function of temperature driven by magnetic ordering or correlation. However, because there are no indications in the published band structure of $Nd_2Ir_2O_7$ (refs. [1,23,38]) that at $T=0$ the electron and hole pockets should touch at E_F, we infer that the free carrier optical conductivity of $Nd_2Ir_2O_7$ is collective and that, due to limitations on the number of collective degrees of freedom, the associated entropy is small. This state of affairs is present in superconductors that are known to be heat insulators while being perfect charge conductors. Another case is presented by charge density waves (CDWs), where collective current transport can be accommodated by sliding of the CDW[39]. However, neither the superconducting nor the CDW scenario is compatible with the observed T^2 dependence of the zero energy spectral weight. Recently, Morimoto and Nagaosa[7] predicted that a Weyl metal with a nonlocal electron–electron interaction in the limit of forward scattering becomes a gapped Weyl Mott insulator. Due to thermal activation across the insulator gap, one expects the intensity of the Drude peak and of the entropy to be non-zero and that both of them follow an Arrhenius-type temperature dependence, which is incompatible with our data. However, this model also predicts a gapless continuum of collective (electron–hole) excitations at $q=0$ and Morimoto and Nagaosa conjecture that for realistic interactions this turns into a collective mode with a linear dispersion. Such a generalization would be extremely interesting in view of its consequences for the optical conductivity and entropy.

We observed a T^2 temperature dependence of the weight of the zero-energy mode in $Nd_2Ir_2O_7$ without the corresponding T^3 contribution to the entropy. This poses a challenge to single-particle band-structure approaches, as it indicates that the collective sector and the single-particle sector are effectively decoupled.

References

1. Wan, X., Turner, A. M., Vishwanath, A. & Savrasov, S. Y. Topological semimetal and Fermi-arc surface states in the electronic structure of pyrochlore iridates. *Phys. Rev. B* **83**, 205101 (2011).
2. Tian, Z. et al. Field-induced quantum metal–insulator transition in the pyrochlore iridate $Nd_2Ir_2O_7$. *Nat. Phys.* **12**, 134–138 (2016).
3. Armitage, N. P., Mele, E. J. & Vishwanath, A. Weyl and Dirac semimetals in three-dimensional solids. *Rev. Mod. Phys.* **90**, 015001 (2018).
4. Ohtsuki, T. et al. Strain-induced spontaneous Hall effect in an epitaxial thin film of a Luttinger semimetal. *Proc. Natl Acad. Sci. USA* **116**, 8803–8808 (2019).
5. Pesin, D. & Balents, L. Mott physics and band topology in materials with strong spin–orbit interaction. *Nat. Phys.* **6**, 376–381 (2010).
6. Moon, E.-G., Xu, C., Kim, Y. B. & Balents, L. Non-Fermi-liquid and topological states with strong spin–orbit coupling. *Phys. Rev. Lett.* **111**, 206401 (2013).
7. Morimoto, T. & Nagaosa, N. Weyl Mott insulator. *Sci. Rep.* **6**, 19853 (2016).
8. Dzero, M., Sun, K., Galitski, V. & Coleman, P. Topological Kondo insulators. *Phys. Rev. Lett.* **104**, 106408 (2010).
9. Kim, D. J., Xia, J. & Fisk, Z. Topological surface state in the Kondo insulator samarium hexaboride. *Nat. Mater.* **13**, 466–470 (2014).
10. Nakatsuji, S., Kiyohara, N. & Higo, T. Large anomalous Hall effect in a non-collinear antiferromagnet at room temperature. *Nature* **527**, 212–215 (2015).
11. Kuroda, K. et al. Evidence for magnetic Weyl fermions in a correlated metal. *Nat. Mater.* **16**, 1090–1095 (2017).
12. Lai, H.-H., Grefe, S. E., Paschen, S. & Si, Q. Weyl–Kondo semimetal in heavy-fermion systems. *Proc. Natl Acad. Sci. USA* **115**, 93–97 (2018).
13. Xu, Y., Yue, C., Weng, H. & Dai, X. Heavy Weyl fermion state in $CeRu_4Sn_6$. *Phys. Rev. X* **7**, 011027 (2017).
14. Kondo, T. et al. Quadratic Fermi node in a 3D strongly correlated semimetal. *Nat. Commun.* **6**, 10042 (2015).
15. Cheng, B. et al. Dielectric anomalies and interactions in the three-dimensional quadratic band touching Luttinger semimetal $Pr_2Ir_2O_7$. *Nat. Commun.* **8**, 2097 (2017).
16. Tomiyasu, K. et al. Emergence of magnetic long-range order in frustrated pyrochlore $Nd_2Ir_2O_7$ with metal–insulator transition. *J. Phys. Soc. Jpn* **81**, 034709 (2012).
17. Guo, H. et al. Magnetic order in the pyrochlore iridate $Nd_2Ir_2O_7$ probed by muon spin relaxation. *Phys. Rev. B* **88**, 060411 (2013).
18. Sagayama, H. et al. Determination of long-range all-in-all-out ordering of Ir^{4+} moments in a pyrochlore iridate $Eu_2Ir_2O_7$ by resonant X-ray diffraction. *Phys. Rev. B* **87**, 100403 (2013).
19. Ma, E. Y. et al. Mobile metallic domain walls in an all-in-all-out magnetic insulator. *Science* **350**, 538–541 (2015).
20. Donnerer, C. et al. All-in-all-out magnetic order and propagating spin waves in $Sm_2Ir_2O_7$. *Phys. Rev. Lett.* **117**, 037201 (2016).
21. Chun, S. H. et al. Magnetic excitations across the metal–insulator transition in the pyrochlore iridate $Eu_2Ir_2O_7$. *Phys. Rev. Lett.* **120**, 177203 (2018).
22. Go, A., Witczak-Krempa, W., Jeon, G. S., Park, K. & Kim, Y. B. Correlation effects on 3D topological phases: from bulk to boundary. *Phys. Rev. Lett.* **109**, 066401 (2012).
23. Witczak-Krempa, W. & Kim, Y. B. Topological and magnetic phases of interacting electrons in the pyrochlore iridates. *Phys. Rev. B* **85**, 045124 (2012).
24. Witczak-Krempa, W., Go, A. & Kim, Y. B. Pyrochlore electrons under pressure, heat, and field: shedding light on the iridates. *Phys. Rev. B* **87**, 155101 (2013).
25. Shinaoka, H., Hoshino, S., Troyer, M. & Werner, P. Phase diagram of pyrochlore iridates: all-in-all-out magnetic ordering and non-Fermi-liquid properties. *Phys. Rev. Lett.* **115**, 156401 (2015).

26. Ueda, K. et al. Magnetic-field induced multiple topological phases in pyrochlore iridates with Mott criticality. *Nat. Commun.* **8**, 15515 (2017).
27. Ueda, K. et al. Variation of charge dynamics in the course of metal–insulator transition for pyrochlore-type $Nd_2Ir_2O_7$. *Phys. Rev. Lett.* **109**, 136402 (2012).
28. Ueda, K., Fujioka, J. & Tokura, Y. Variation of optical conductivity spectra in the course of bandwidth-controlled metal–insulator transitions in pyrochlore iridates. *Phys. Rev. B* **93**, 245120 (2016).
29. Sushkov, A. B. et al. Optical evidence for a Weyl semimetal state in pyrochlore $Eu_2Ir_2O_7$. *Phys. Rev. B* **92**, 241108 (2015).
30. Machida, Y., Nakatsuji, S., Onoda, S., Tayama, T. & Sakakibara, T. Time-reversal symmetry breaking and spontaneous Hall effect without magnetic dipole order. *Nature* **463**, 210–213 (2010).
31. Tabert, C. J. & Carbotte, J. P. Optical conductivity of Weyl semimetals and signatures of the gapped semimetal phase transition. *Phys. Rev. B* **93**, 085442 (2016).
32. Tabert, C. J., Carbotte, J. P. & Nicol, E. J. Optical and transport properties in three-dimensional Dirac and Weyl semimetals. *Phys. Rev. B* **93**, 085426 (2016).
33. Lide, D. R. *CRC Handbook of Chemistry and Physics* 71st edn (CRC Press, 1990).
34. Hosur, P., Parameswaran, S. A. & Vishwanath, A. Charge transport in Weyl semimetals. *Phys. Rev. Lett.* **108**, 046602 (2012).
35. Zaanen, J. Planckian dissipation, minimal viscosity and the transport in cuprate strange metals. *SciPost Phys.* **6**, 061 (2019).
36. Watahiki, M. et al. Crystalline electric field study in the pyrochlore $Nd_2Ir_2O_7$ with metal–insulator transition. *J. Phys. Conf. Ser.* **320**, 012080 (2011).
37. Phillips, P. Mottness. *Ann. Phys.* **321**, 1634–1650 (2006).
38. Wang, R., Go, A. & Millis, A. Weyl rings and enhanced susceptibilities in pyrochlore iridates: $k{\cdot}p$ analysis of cluster dynamical mean-field theory results. *Phys. Rev. B* **96**, 195158 (2017).
39. Grüner, G. The dynamics of charge-density waves. *Rev. Mod. Phys.* **60**, 1129–1181 (1988).

Methods

Sample synthesis. Single crystals of $Nd_2Ir_2O_7$ were grown with the flux method using polycrystalline powder and KF flux described in ref. [40]. The crystal used for this study had a weight of 1.83 mg, thickness of 0.4 mm and a trapezium-shaped 0.5-mm² surface area that was used for the optical experiments.

Magnetic susceptibility experiments. ZFC and FC magnetization was measured as a function of temperature using the vibrating sample mode of a superconducting quantum interference device magnetometer (Quantum Design MPMS). The vibrating sample mode frequency was set to 14 Hz. For the ZFC measurement, the sample was cooled from room temperature to 4 K without any applied field. At low temperature, a magnetic field of 1,000 Oe was applied and the magnetization was measured while warming at a constant rate of 0.45 K min^{-1}. For the FC measurement, the sample was cooled in a field and the data were collected in the same conditions as for ZFC.

The susceptibility of a system of n paramagnetic ions per unit volume is given by the Curie law:

$$\chi(T) = \frac{np^2\mu_B^2}{3k_BT} \tag{1}$$

where p is the effective moment. Vice versa, if there is no coupling between the moments, the effective moment $p(T)$, defined as

$$p(T) \equiv \sqrt{\frac{3k_BT\chi(T)}{n\mu_B^2}} \tag{2}$$

should be independent of temperature. The quantity $p(T)^2$ is displayed in Fig. 1a.

D.c. transport experiments. The d.c. resistivity was measured in the temperature range from 1.8 to 300 K using a Quantum Design physical property measurement system in four-point geometry with an excitation current of 0.5 mA. Electric contacts on the samples were made using silver paste. The resistivity was calculated from the resistance using sample thickness, width and the distance between the contacts. Comparison with the optical $\sigma(\omega,t)$ extrapolated to $\omega = 0$ showed a lower value than the conductivity measured with the four-point method at all temperatures. Because the contact layout on a small sample may result in an overall scaling of the resistivity, and because the optical conductivity at 300 K is frequency-independent in the far-infrared, we used the optical $\sigma(\omega,300\,\mathrm{K})$ (see next section) extrapolated to $\omega = 0$ to calibrate the d.c. resistivity shown in Fig. 1a.

Optical measurements and data analysis. We measured the near normal reflectivity $|r(\omega)|^2$ for {5 meV; 1.5 eV} with a Fourier-transform spectrometer combined with an ultra-high vacuum flow cryostat, using in situ gold evaporation for calibrating the signal. These data are displayed in Extended Data Fig. 1. In the energy range {0.5 eV; 3 eV} we measured the complex dielectric function $\epsilon(\omega) = \epsilon_1(\omega) + i\epsilon_2(\omega)$ using ellipsometry of the a–b plane of our samples at an incident angle of 65° relative to the normal. The result is displayed in Extended Data Fig. 2. From $\epsilon(\omega)$ we calculated amplitude $|r|$ and phase ϕ of the normal incidence reflectivity using the Fresnel equation, providing an excellent match with the aforementioned reflectivity data. Fitting $|r(\omega)|$ and $\phi(\omega)$ simultaneously with a Drude–Lorentz expansion of $\epsilon(\omega)$ provided extrapolations of $|r(\omega)|$ in the ranges {0; 5 meV} and {3 eV; ∞}. Application of the Kramers–Kronig relation to $\ln(|r(\omega)|)$ in the range {0; ∞} provided the phase spectrum $\phi(\omega)$ at all frequencies, in particular in the range {5 meV; 0.5 eV} where the phase was not measured using ellipsometry. The complex dielectric function $\epsilon(\omega)$ and the optical conductivity $4\pi\sigma_1(\omega) = \omega\epsilon_2(\omega)$ were calculated in the entire range of the experimental data, using the Fresnel equation for the reflection coefficient. The effective particle number in the primitive cell (two formula units, four Ir ions) of volume $V_{pc} = 2.79 \times 10^{-22}\,\mathrm{cm}^3$ was calculated using the expression

$$N_{\mathrm{eff}}(\omega) = \frac{2m_eV_{pc}}{\pi e^2}\int_0^{\omega}\sigma_1(\omega')\mathrm{d}\omega' \tag{3}$$

Specific heat experiments. The specific heat of the $Nd_2Ir_2O_7$ single crystal was obtained using a Quantum Design physical property measurement system with the heat capacity relaxation technique from 5 K to 55 K in increments of 1 K with a temperature relaxation amplitude of 1% of the base temperature (for example, at 10 K the temperature relaxation amplitude is ~0.1 K). We first measured the empty heat capacity puck with a small amount of Apiezon N grease (used for glueing the sample with good thermal contact) to extract the heat capacity of the platform + Apiezon N grease, $C_{add}(T)$. We then added the sample and measured the total heat capacity $C_{tot}(T)$. This provided the heat capacity of the sample $C_{sample}(T) = C_{tot}(T) - C_{add}(T)$. Using the mass of the sample $M = 1.830 \pm 0.005$ mg and the molar mass per $Nd_2Ir_2O_7$ formula unit $M_{fu} = 784.92\,\mathrm{g\,mol}^{-1}$, we calculated the molar specific heat $C(T) = C_{sample}(T)M_{fu}/M$. Because the primitive cell contains two formula units of $Nd_2Ir_2O_7$, the specific heat per primitive cell is, in units of k_B, $c(T) = 2C(T)/R$, where R is the gas constant. The entropy per primitive cell (in units of k_B) is calculated from the specific heat using

$$s(T) = \int_0^T \frac{c(T')}{T'}\mathrm{d}T' \tag{4}$$

The experimental specific heat data in the range 5–40 K (Fig. 1c) was fitted to the the sum of a vibrational contribution cv (equation (6)) and a Schottky contribution c_f (equation (9))

$$c(T) = c_f(T) + c_v(T) \tag{5}$$

We have fitted the experimental data from 5 to 40 K, fixing $T_N = 37$ K and $\eta = 2$. This provided the parameters Δ_0, a_3 and a_5 (see next section).

Theoretical expressions for the phonon specific heat. To model the vibrational contribution to the specific heat we use

$$c_v(T) = a_3T^3 - a_5T^5 \tag{6}$$

The parameters a_3 and a_5 effectively subsume—for the relevant range of temperatures—the thermodynamic properties of all vibrational modes (3 acoustic and 63 optical) in the primitive cell.

Theoretical expressions for the specific heat of the localized Nd 4*f* electrons. We assume that the Ir sublattice induces an exchange field at the Nd site causing the ground-state doublet to split with an energy difference Δ (ref. [41]). The entropy per primitive cell (in units of k_B) is

$$s_f(T) = 4\left[\frac{\ln\left(1+\mathrm{e}^{-\Delta/T}\right)}{1+\mathrm{e}^{-\Delta/T}} + \frac{\ln\left(1+\mathrm{e}^{\Delta/T}\right)}{1+\mathrm{e}^{\Delta/T}}\right] \tag{7}$$

where the factor of 4 in the right-hand side accounts for the fact that each primitive cell contains four Nd^{3+} ions. We assume $\Delta = 0$ for $T > T_N$ and below T_N we adopt the following approximation for the temperature dependence:

$$\Delta = \Delta_0\sqrt{1 - \left(\frac{T}{T_N}\right)^{\eta}} \tag{8}$$

The relation $c_f(T) = Tds_f/\mathrm{d}T$ then gives the specific heat per primitive cell:

$$c_f(T) = 4\frac{\mathrm{e}^{\Delta/T}}{\left(\mathrm{e}^{\Delta/T}+1\right)^2}\left[\frac{\Delta^2}{T^2} + \eta\frac{\Delta_0^2}{2}\frac{T^{\eta-2}}{T_N^{\eta}}\right] \tag{9}$$

To provide a quantitative insight into the expected jump at T_N associated with the entropy of Nd^{3+} moments, we calculate the exchange potential at the Nd sites, the entropy and the specific heat for two sets of parameters. For the exchange potential at the Nd sites we use equation (8). The entropy and specific heat are calculated with equations (7) and (9). In Extended Data Fig. 3 we show two cases: $\Delta_0 = 6.5$ K, $T_N = 37$ K (left panels) and $\Delta_0 = 15$ K, $T_N = 30$ K (right panels), which correspond to the two samples shown in Fig. 1c. The jump at T_N in the left panel is very small and falls within the noise of the specific heat data obtained in the single crystal shown Fig. 1c. On the other hand, the jump in the right panel is quite pronounced and is of the order of magnitude of the experimental data obtained on the polycrystalline samples shown in Fig. 1c.

Theoretical expressions for the itinerant Ir 5*d* electronic specific heat. The specific heat and entropy per primitive cell corresponding to g Weyl nodes, in units of k_B, are

$$c_W(T) = gV_{pc}\left(\frac{k_BT}{\hbar v}\right)^3\frac{4}{\pi^2}\int_0^{\infty}\frac{x^3}{\mathrm{e}^x+1}\mathrm{d}x \tag{10}$$

$$s_W(T) = \frac{g}{3}V_{pc}\left(\frac{k_BT}{\hbar v}\right)^3\frac{4}{\pi^2}\int_0^{\infty}\frac{x^3}{\mathrm{e}^x+1}\mathrm{d}x \tag{11}$$

where V_{pc} is the volume of the primitive cell (two formula units of $Nd_2Ir_2O_7$). For the electronic contribution of the Ir 5*d* states for $T > T_N$ we use the specific heat of a single quadratic band touching point:

$$c_{QBT}(T) = \frac{5\sqrt{2}}{\pi^2}\frac{m^{3/2}V_{pc}}{\hbar^3}(k_BT)^{3/2}\int_0^{\infty}\frac{x^{3/2}}{\mathrm{e}^x+1} \tag{12}$$

We use $m \approx 6.3m_0$ where m_0 is the free electron mass, which is obtained from fitting angle-resolved photoemission spectroscopy data of $Pr_2Ir_2O_7$ (refs. [14,15]), a compound that is paramagnetic at all temperatures. To describe the second-order

transition from Weyl semimetal to paramagnetic QBT semimetal, for $T \leq T_N$ we use

$$s(T) = s_W(T) + (T/T_N)^{\eta}[s_{QBT}(T) - s_W(T)] \quad (13)$$

so that $s(0) = s_W(0)$ and $s(T_N) = s_{QBT}(T_N)$. For $s_W(T)$ we use equation (11), taking $\upsilon = 41\,\mathrm{km\,s^{-1}}$ and $g = 24$. In Extended Data Fig. 4 we use $\eta = 2$. Taking a larger value, for example $\eta = 4$, does not significantly change the outcome. The entropy described by equation (13) is continuous at all temperatures, and it has a change of slope at T_N corresponding to a (negative) jump in the specific heat $c = T\mathrm{d}s/\mathrm{d}T$ at T_N.

Theoretical expressions for the optical properties of Weyl nodes. We summarize the expressions derived in refs. [31,32], which we use in the discussion of this paper. The $T = 0$ optical conductivity of a 3D Dirac semimetal is

$$\sigma_1(\omega) = \frac{\alpha}{24\pi}\frac{gc}{\upsilon}\omega \quad (14)$$

where $\alpha = 1/137$ is the fine-structure constant, g is the number of Dirac cones, c is the velocity of light and υ is the Dirac velocity. The temperature dependence of the free carrier spectral weight is

$$\omega_p(T)^2 = \omega_p(0)^2 + \frac{2\pi\alpha}{9}\frac{gc}{\upsilon}(k_B T)^2 \quad (15)$$

Moving the chemical potential μ away from the Dirac point results in a carrier density

$$n_0 = \frac{g\mu^3}{6\pi^2\hbar^3\upsilon^3} \quad (16)$$

and a residual Drude spectral weight

$$\omega_p(0)^2 = \left(\frac{32\pi g n_0^2}{3}\right)^{1/3}\alpha c\upsilon \quad (17)$$

Estimate and comparison of all contributions to the specific heat. To provide a quantitative comparison of the relative strength of the various different contributions to the specific heat we show in Extended Data Fig. 4 the experimental data of $Nd_2Ir_2O_7$ together with the calculated contributions from (1) phonons, (2) the itinerant Ir 5*d* electrons and (3) the Nd local moments. For the vibrational contribution we use the ab initio calculations for the isostructural compound $Tb_2Ti_2O_7$ from ref. [42]. The specific heat contribution from the Nd ions (four per primitive cell) was calculated using equation (9). For the exchange potential at the Nd sites we use equation (8) with $T_N = 37\,\mathrm{K}$, $\Delta_0 = 6.5\,\mathrm{K}$ and $\eta = 2$. From Extended Data Fig. 4 we make the following observations: (1) below 15 K the specific heat is dominated by the Schottky term; (2) above 15 K the specific heat is dominated by the phonon part; (3) for all temperatures the contribution of the itinerant Ir 5*d* electrons is at least two orders of magnitude below the combined Schottky plus phonon part.

Data availability

The datasets generated and analysed during the current study are available in ref. [43]. These will be preserved for 10 years. All other data that support the plots within this paper and other findings of this study are available from the corresponding author upon reasonable request.

References

40. Ishikawa, J. J., O'Farrell, E. C. T. & Nakatsuji, S. Continuous transition between antiferromagnetic insulator and paramagnetic metal in the pyrochlore iridate $Eu_2Ir_2O_7$. *Phys. Rev. B* **85**, 245109 (2012).
41. Chen, G. & Hermele, M. Magnetic orders and topological phases from *f–d* exchange in pyrochlore iridates. *Phys. Rev. B* **86**, 235129 (2012).
42. Ruminy, M. et al. First-principles calculation and experimental investigation of lattice dynamics in the rare-earth pyrochlores $R_2Ti_2O_7$ (R = Tb, Dy, Ho). *Phys. Rev. B* **93**, 214308 (2016).
43. *Optics, Transport, Specific Heat and Magnetic Susceptibility of the Correlated Semimetal $Nd_2Ir_2O_7$* (Yareta, 2020); https://doi.org/10.26037/yareta:3k2uscc2bjbqdisikigdjcx2lm

Acknowledgements

D.v.d.M. acknowledges insightful discussions with D. Abanin and N. Nagaosa. This project was supported by the Swiss National Science Foundation (project no. 200020-179157). This work is partially supported by CREST (JPMJCR18T3), the Japan Science and Technology Agency (JST), by Grants-in-Aids for Scientific Research on Innovative Areas (15H05882 and 15H05883) from the Ministry of Education, Culture, Sports, Science and Technology of Japan and by Grants-in-Aid for Scientific Research (19H00650). Work at JHU was supported through the Institute for Quantum Matter, an EFRC funded by the US DOE, Office of BES (DE-SC0019331).

Author contributions

K.W., B.X., C.W.R., N.B., B.M. and J.T. performed experiments. Y.Q., T.O., B.C. and S.N. prepared samples. K.W., N.B., B.M. and D.v.d.M. analysed data. N.P.A. and D.v.d.M. planned the project. K.W. and D.v.d.M. wrote the manuscript with input and comments from all other authors.

Competing interests

The authors declare no competing interests.

Additional information

Extended data is available for this paper

Correspondence and requests for materials should be addressed to D.v.d.M.

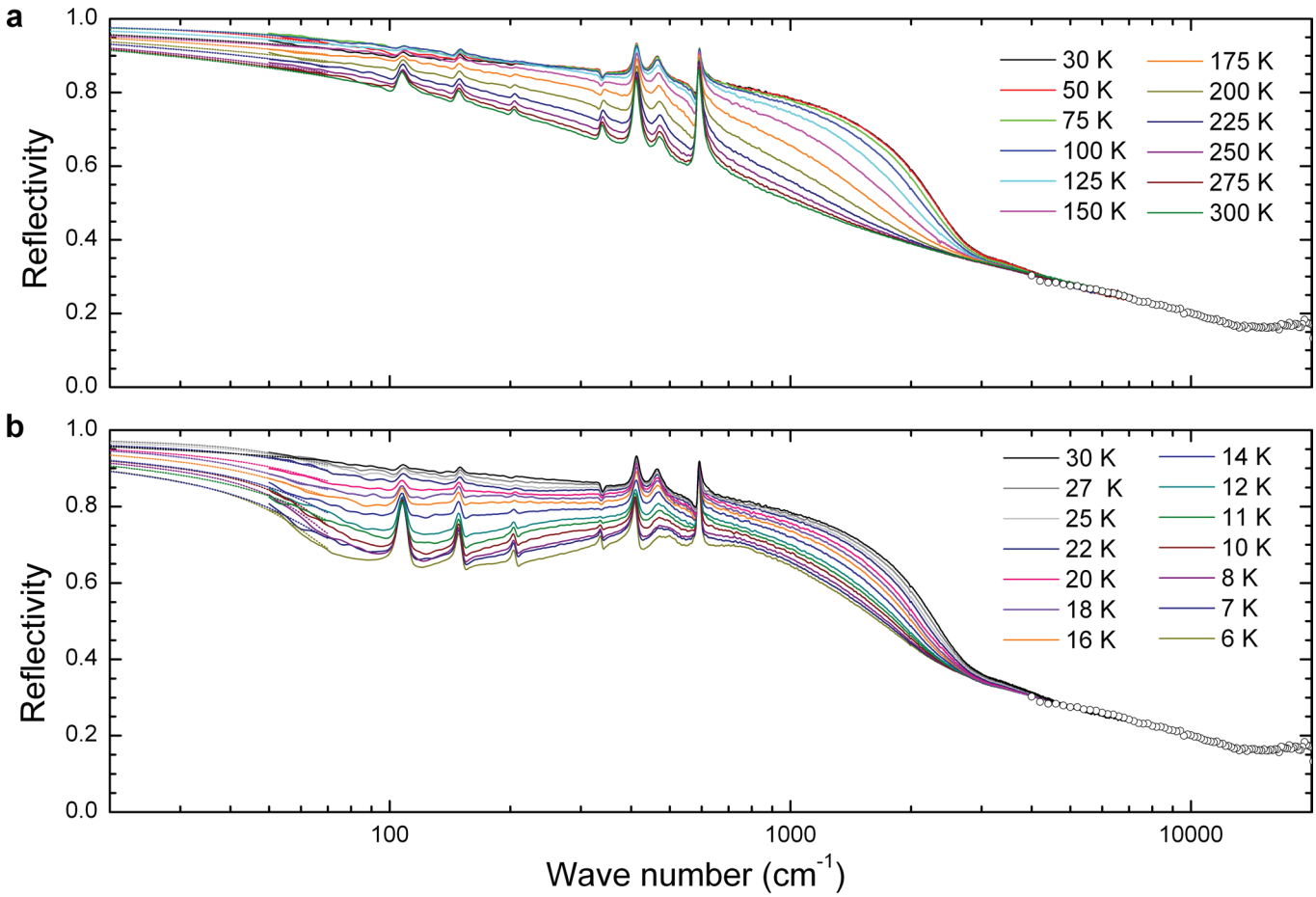

Extended Data Fig. 1 | Reflectance spectra. Solid curves: Near normal incidence reflectivity, $R=|r|^2$, of $Nd_2Ir_2O_7$ for selected temperatures. Dotted curves below 50 cm^{-1}: Extrapolations using simultaneous Drude–Lorentz fitting to the reflectance spectra and the ellipsometric data beween 4000 and 18000 cm^{-1} of Extended Data Fig. 2. **a**, Between 30 and 300 K. **b**, Between 6 and 30 K.

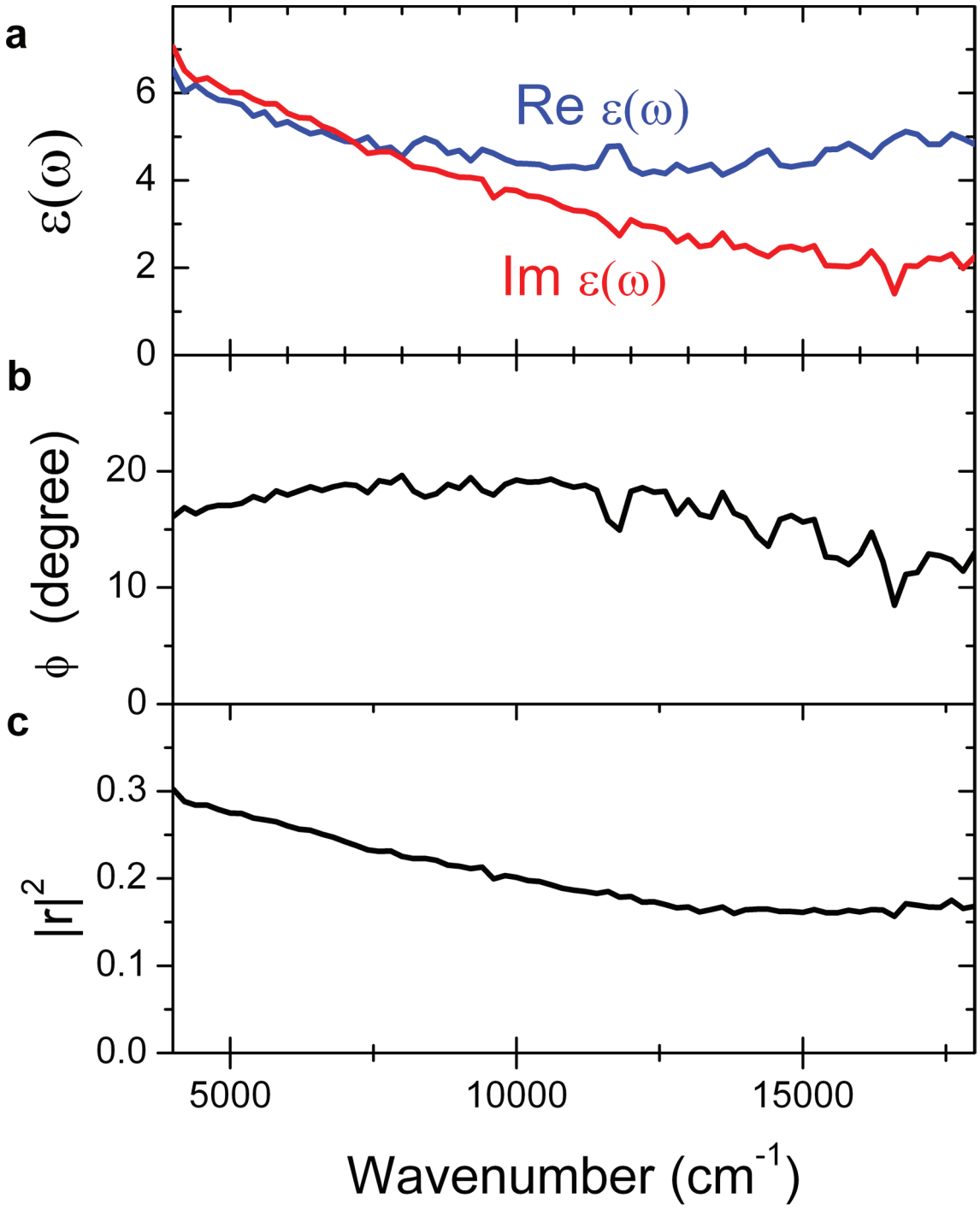

Extended Data Fig. 2 | Ellipsometric data between 4000 and 18000 cm^{-1}. a, Real and imaginary part of the dielectric function at room temperature measured using spectroscopic ellipsometry at $\theta = 65$ degrees with the surface normal. **b**, Phase of the normal incidence reflection coefficient using the Fresnel equation $|r|e^{i\phi} = (1-\sqrt{\varepsilon})/(1+\sqrt{\varepsilon})$. **c**, Absolute square of the reflection coefficient.

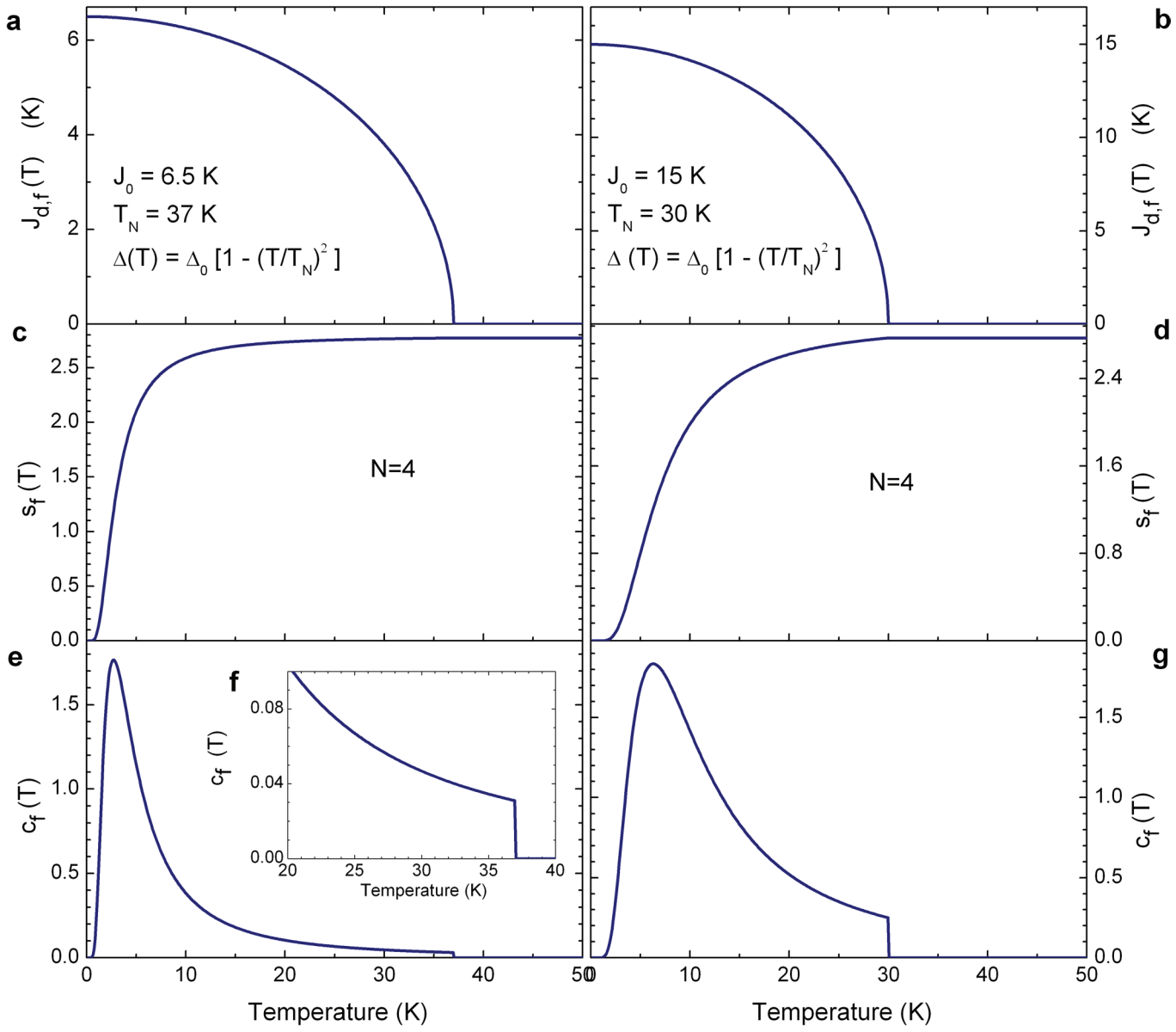

Extended Data Fig. 3 | Thermodynamic properties of the Nd 4f states. Model calculation of the exchange potential at the Nd sites $\Delta(T)$, entropy per primitive cell $s_f(T)$, and specific heat per primitive cell $c_f(T)$ (see Methods). **a,c,e,f**, Δ_0 =6.5 K and T_N=37 K. **b,d,g**, Δ_0 =15 K and T_N =30 K.

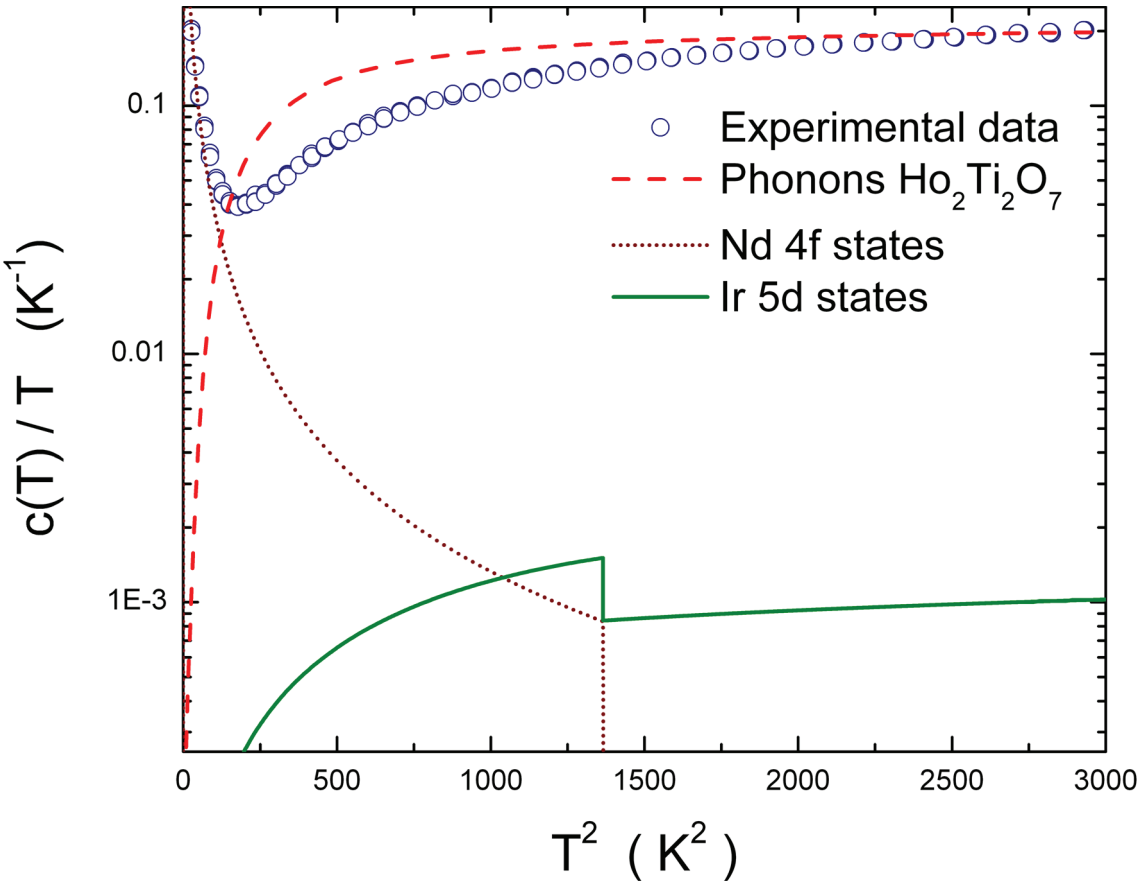

Extended Data Fig. 4 | Comparison of the contributions to the specific heat per primitive cell. Experimental specific heat per primitive cell of $Nd_2Ir_2O_7$. Red curve: Calculated phonon contribution (see Methods). Olive curve: Calculated contribution of the itinerant Ir 5d band electrons (see Methods). Brown curve: The contribution from the localized Nd 4f electrons (see Methods).